Research Article Vol. 8, No. 2 / February 2021 / Optica 249

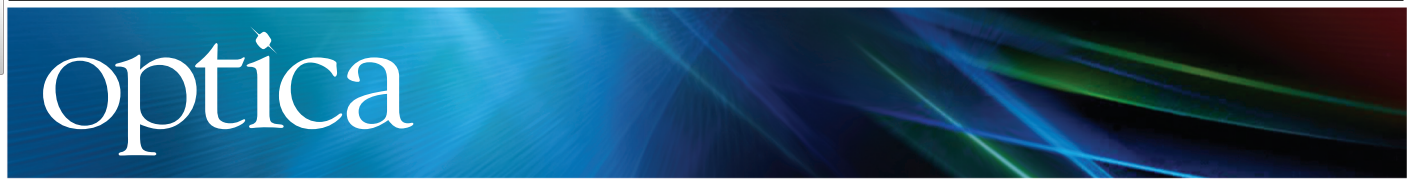

Veselago lensing with Weyl metamaterials

Yang Yang,[1,2,†] Yangang Bi,[1,†] Liang Peng,[1,3] Biao Yang,[4] Shaojie Ma,[1,5] Hsun-Chi Chan,[1,5] Yuanjiang Xiang,[6,9] and Shuang Zhang[1,7,8,10]

[1]School of Physics & Astronomy, University of Birmingham, Birmingham B15 2TT, UK
[2]State Key Laboratory of Information Photonics and Optical Communications, School of Science, Beijing University of Posts and Telecommunications, Beijing 100876, China
[3]School of Electronics and Information, Hangzhou Dianzi University, Hangzhou 310018, China
[4]College of Advanced Interdisciplinary Studies, National University of Defense Technology, Changsha 410073, China
[5]Institute of Microscale Optoelectronics (IMO), Shenzhen University, Shenzhen 518060, China
[6]Key Laboratory for Micro/Nano Optoelectronic Devices of Ministry of Education, School of Physics and Electronics, Hunan University, Changsha, 410082, China
[7]Department of Physics, University of Hong Kong, Hong Kong, China
[8]Department of Electrical & Electronic Engineering, University of Hong Kong, Hong Kong, China
[9]e-mail: xiang78@hnu.edu.cn
[10]e-mail: shuzhang@hku.hk

Received 24 August 2020; revised 18 November 2020; accepted 13 January 2021 (Doc. ID 406167); published 16 February 2021

Negative refraction is an exotic optical phenomenon that is usually observed at the interface between a positive-index material and a negative-index, or "left-handed" material. One direct application of negative refraction is the Veselago lens, a flat lens that can focus the light emitted by a point source located on one side of the negative index medium onto the opposite side. Besides negative-index materials, Veselago lensing effect has been observed with two-dimensional crystals possessing Dirac points, such as graphene for electrons. Here we observe all-angle negative refraction and Veselago imaging in three dimensions with a Type I Weyl metamaterial. Furthermore, our ideal Weyl metamaterial exhibits remarkable spin-selective transmission around the Weyl frequency that arises from its intrinsic chiral optical response. Our results show that the ideal Weyl metacrystal provides a versatile platform for lensing applications and novel photon-spin selective devices.

https://doi.org/10.1364/OPTICA.406167

1. INTRODUCTION

In 1968, Veselago theoretically predicted negative refraction of electromagnetic waves at the interface between a positive-index material and a "left-handed" medium [1]. The left-handed medium had been considered to be unphysical, and therefore the Veselago lens had gone unnoticed until the concept of metamaterials was proposed about two decades ago. Since then, tremendous effort has been dedicated to the realization of functional materials with negative refraction, in which light propagates with phase and energy velocities opposing each other. Pendry further extended the concept, theoretically showing that a flat slab of lossless negative-index material can serve as a perfect lens for imaging with subdiffraction-limited resolution [2,3]. Negative refraction has been explored in various systems, such as negative-index metamaterials [4–10], photonic crystals [11,12], surface plasmons [13–15] and hyperbolic metamaterials [16–18].

Recently, topological phases such as topological insulators and topological semimetals have come into focus, since these nontrivial topological materials support surface states that are immune from scattering. While initially studied in condensed matter systems [19–21], the concept of topological physics has been extended to classical systems such as photonics and acoustics, leading to the realization of various topological systems such as photonic topological insulators and gapless topological phases of photonic Dirac and Weyl points [22–46]. As a highly robust gapless topological state, Weyl points are the discrete crossings of linearly dispersing energy bands in three-dimensional (3D) momentum space. They can be viewed as monopoles of quantized monopole charge in the momentum space, by which the sign of the monopole charge is determined by the Weyl point's chirality. Various interesting observables have been proposed or demonstrated, including the existence of Fermi arcs at the interfaces [21,28–40], diverging or diminishing scattering cross sections and enhanced or suppressed Purcell effect at the Weyl frequency [47,48], handedness-dependent Imbert–Fedorov shift [49,50], and chiral zero modes and the associated magneto-resistance and chiral magnetic effects [51,52]. It has also been proposed that below the Weyl frequency, negative refraction can occur at the interface of a suitably designed Weyl material and a normal dielectric medium [33]. Due to the 3D nature, the negative refraction in a Weyl medium resembles that in a 3D isotropic negative-index material, while the design and fabrication of the latter has posed great challenges due to the requirement of negative electric and

magnetic responses in all directions. Here, we experimentally realize Veselago lens in an ideal photonic Weyl metamaterial, which is a key signature of all-angle negative refraction in a 3D setting. Due to the robustness and linear dispersion of the Weyl medium, the Weyl approach towards negative refraction provides major advantages over traditional negative-index media such as low loss and better impedance matching at the interface to ensure higher transmission.

2. THEORY AND EXPERIMENTAL REALIZATION OF VESELAGO LENSING

Close to the Weyl frequency, the dispersion of Weyl media can be described by a simple two-band model involving all three Pauli matrices linearly coupled to the three wave vectors along orthogonal directions, with the general form of the effective Hamiltonian expressed as

$$H_{\text{eff}} = V_x k_x \sigma_x + V_y k_y \sigma_y + V_z k_z \sigma_z + W_x k_x I, \qquad (1)$$

where $\sigma_{x,y,z}$ are Pauli matrices, I is a 2×2 identity matrix, $V_{x,y,z}$ are the Fermi velocities, and W_x is the tilted velocity of the Weyl point along the x direction. The tilting of the Weyl dispersion cone is determined by the Weyl parameter $\alpha_{\text{Weyl}} = W_x/V_x$, with $\alpha_{\text{Weyl}} < 1$ corresponding to Type I Weyl systems, and $\alpha_{\text{Weyl}} > 1$ corresponding to Type II Weyl systems [53]. A Type I Weyl system features a shrinking equifrequency surface (EFS) and diminishing density of states towards the Weyl frequency, which provides a unique platform for exploring a variety of intriguing physical phenomena.

The realistic design of the Weyl system for demonstrating negative refraction is based on an ideal photonic Weyl metamaterial with broken inversion symmetry [31], which exhibits four Weyl points at the same energy; they are well separated from any other bands. The unit cell geometry of the ideal Weyl metamaterial is shown in Fig. 1(b). A saddle-shaped metallic structure with D_{2d} point group symmetry is embedded in the hosting material with dielectric constant of 2.2. The band structure of the ideal photonic Weyl metacrystal is shown in Fig. 1(c), showing four Type I Weyl points at $\omega_{\text{Weyl}} = 13.5$ GHz formed by the linear crossing along $\Gamma - \text{M}$ between a longitudinal mode (LM) of negative dispersion and a transverse mode (TM) of positive dispersion residing in the same frequency, as protected by the symmetry of the structure. The top surface of the Weyl metamaterial fabricated by a printed circuit board is shown in Fig. 1(a), with the square lattice vectors (u and v) tilted 45° from the x and y axes, while the interface for observing negative refraction lies in the xz plane. Thus, two of the Weyl points of the same chirality are projected onto the center of the surface Brillouin zone, while the other two are projected to two points away from the center by a separation larger than k_0, and therefore are not involved in the following investigation of imaging. Below the Weyl frequency, the Weyl points expand into four elliptical EFSs (blue line) located on the k_x and k_y axis, respectively [Fig. 1(d)]. At the interface between air and the Weyl metamaterial, the tangential component of the momentum is conserved. As a

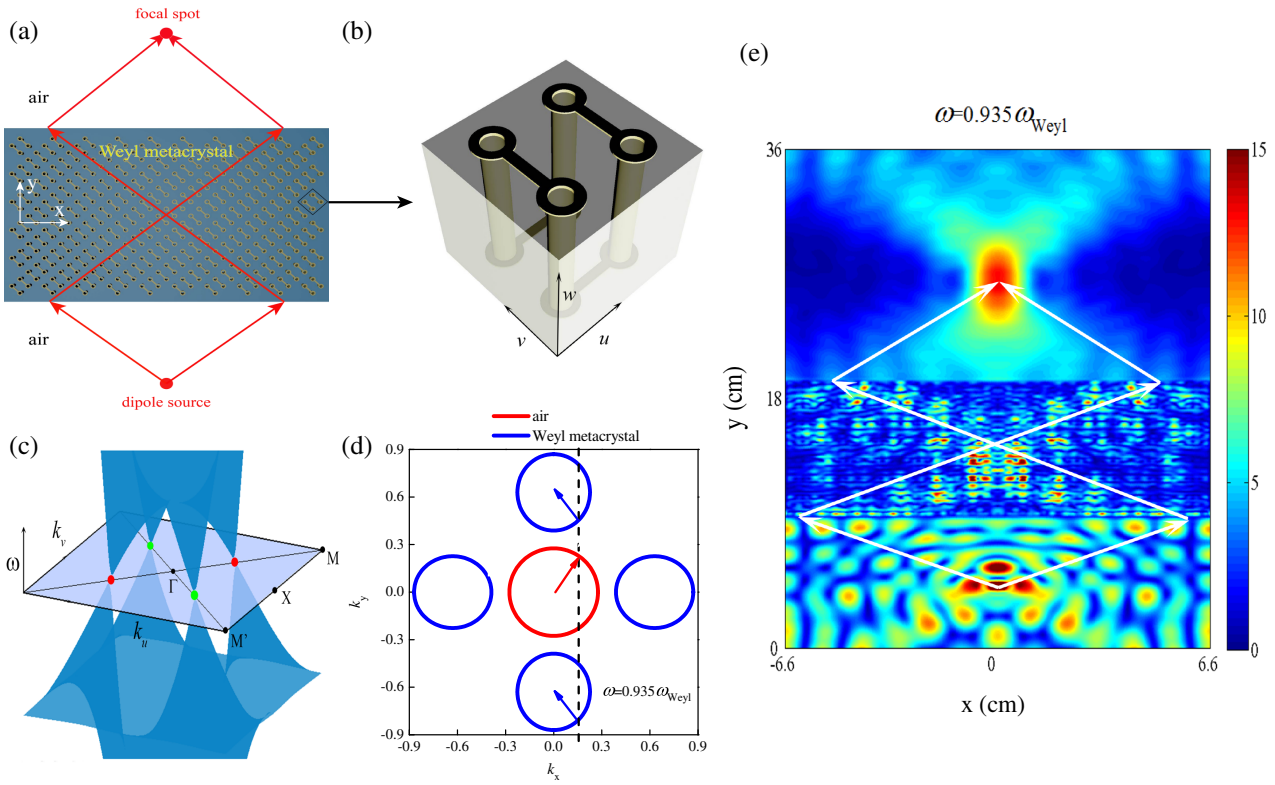

Fig. 1. Negative refraction of the ideal Weyl metacrystal. (a) Schematic configuration of the negative refraction of the ideal Weyl metacrystal with exciting dipole source located in air; (b) unit cell of Weyl metacrystal: a saddle-shaped connective metallic coil that possesses D_{2d} point group symmetry in the tetragonal lattice; the 3D period of the unit structure is $p_u = p_v = 3$ mm and $p_w = 4.5$ mm; (c) band structure of the ideal Weyl metacrystal; four Type I Weyl points reside on the same energy along the $\Gamma - \text{M}$ directions in the $k_z = 0$ plane (purple plane); (d) EFSs of the Weyl metacrystal (blue line) at the frequency of $0.935\omega_{\text{Weyl}}$ in $k_x - k_y$ plane; the red circle in the center represents the EFS of air in the same frequency. The incident and refracted wave vectors are denoted by the blue and red arrows, respectively. (e) Simulated beam profile of the all-angle negative refraction of the ideal Weyl metacrystal at the frequency of $0.935\omega_{\text{Weyl}}$; the white lines indicate the beam propagating direction.

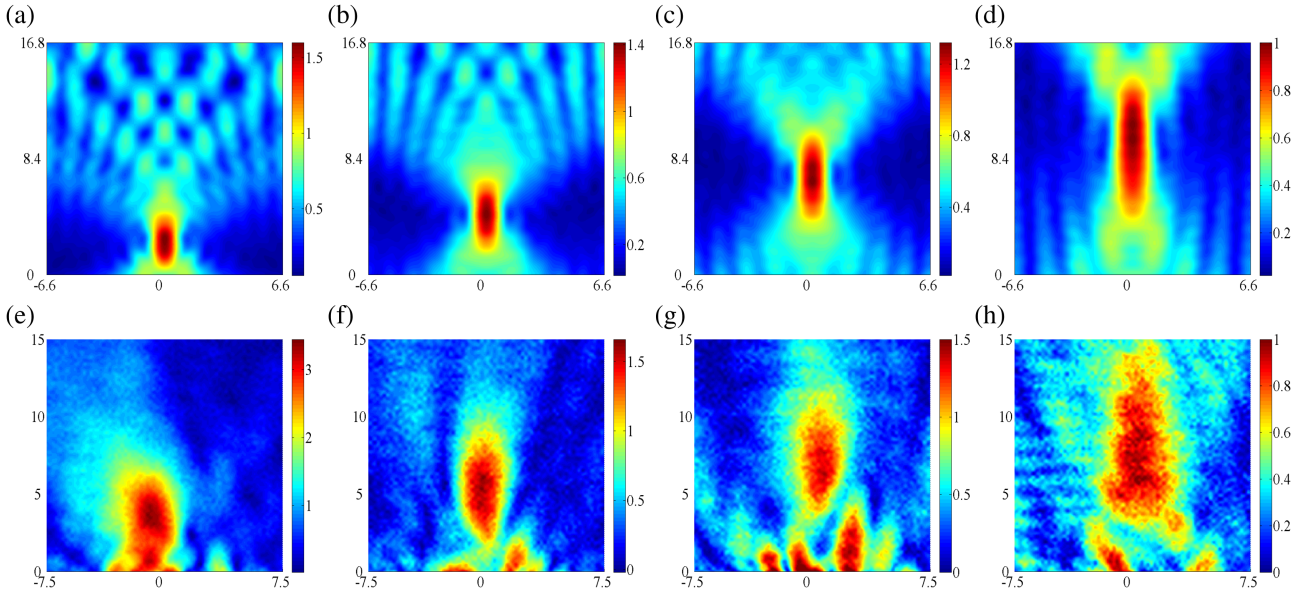

Fig. 2. Evolution of the focusing profile of the transmitted wave through the Weyl metacrystal when the frequency increases to the Weyl frequency. (a)–(d) Full wave simulation; frequencies are (0.921, 0.928, 0.935, 0.942) ω_{Weyl}, respectively; (e)–(i) experimental measurements, frequencies are (0.891, 0.8963, 0.9, 0.9041) ω_{Weyl}, respectively.

result, an incident light from air (red arrow) is expected to experience negative refraction as the group velocity (blue arrow) of the Weyl metamaterial points inward toward the center of the EFSs.

To confirm the negative refraction below the Weyl frequency, we perform a full wave simulation of refraction at the interface between the Weyl metacrystal and air using the commercial software Computer Simulation Technology (CST). The schematic configuration is shown in Fig. 1(a), a dipole source oriented in the z direction is positioned a distance away from the ideal Weyl metacrystal in the air. The distribution of the simulated electric field is illustrated in Fig. 1(e) at $\omega = 0.935\omega_{\text{Weyl}}$. The simulation results clearly show that the field is focused across the Weyl metacrystal to the other side of the metacrystal, indicating all-angle negative refraction at the interface. The white lines indicate the beam propagating direction, showing another focusing point inside the metacrystal.

Close to the Weyl frequency, the size of the EFS of the Weyl metacrystal varies rapidly, and the corresponding effective refractive index is highly dispersive, which strongly varies the focusing features at different frequencies. Evolution of focusing profile of the transmitted wave through the Weyl metacrystal with frequency is shown in Fig. 2: (a)–(d) correspond to full wave simulation results and (e)–(g) are experimental measurements. One can see that the focal spot gradually moves away from the interface and becomes more elongated in the y direction when the frequency increases towards the Weyl frequency. When approaching the Weyl frequency, the focal spot spreads out and the focal length increases towards infinity. While above the Weyl frequency, the effective refractive index becomes positive and the transmitted wave diverges. Our results show that negative refraction occurs in a broad band of frequency range of about 0.75 GHz below the Weyl frequency. The experimental observations are in good agreement with the rigorous simulation results, demonstrating the all-angle negative refraction of the ideal Weyl metacrystal.

Using Fresnel's law, the effective refractive index n_{eff} of Weyl metacrystal can be obtained in the paraxial approximation:

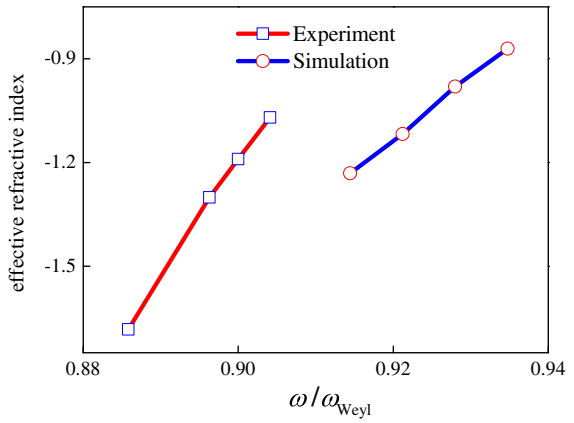

Fig. 3. Variation of the effective refractive index of Weyl metacrystal when the frequency approaches the Weyl frequency. The discrepancy between the theoretical and experimental results comes from the incomplete matching of the experimental sample and simulation setup.

$n_{\text{eff}}/n_{\text{air}} \approx d_2/(d_1 + d_3)$, where d_1 and d_3 are, respectively, the distance of dipole and focal spot to the Weyl metacrystal, d_2 is the thickness of the Weyl metacrystal, and n_{air} is the refractive index of air. The refractive indices of the ideal Weyl metacrystal retrieved from both the simulation and experimental measurement for different frequencies are illustrated in Fig. 3. Due to approximate linear relation of the radius of elliptical EFS of Weyl point with frequency [47], the amplitude of the effective refractive index decreases linearly with the increase of frequency towards the Weyl frequency, which is verified by both the experimental and simulation results. However, there is a relative shift in frequency between the measured and simulated curves of the refractive index, which is due to a slight difference in the geometries between the fabricated sample and the simulated one—to reduce the simulation complexity, the hollow metallic cylinders in Fig. 1(b) are replaced by solid ones.

3. CIRCULAR DICHROISM OF IDEAL WEYL METAMATERIAL

Because the two Weyl cones involved in the refraction have the same topological charge, it is expected that the metamaterial exhibits strong chirality and circular dichroism for the incident beam [54]. Figure 4 shows the simulated and measured transmissions for the incident beam of different circular polarizations through the Weyl metacrystal around the Weyl frequency. As shown by the simulation results in Fig. 4(a), the left-handed circular polarized (LCP) wave experiences a very high transmission around the Weyl frequency (around 90%), while the transmittance for the right-handed circular polarized (RCP) wave is below 10%. In the measurements shown in Fig. 4(b), there is also a large difference between the transmittances of the two circular polarizations. However, due to the imperfection of the sample, the measured transmittances are significantly less than the simulated results for both circular polarizations.

The underlying physical mechanism of the giant spin-selective transmission of the ideal Weyl metamaterial can be understood within the framework of multipole charge–current interaction. Here we look into the electric current distribution for an individual structure when excited by a circularly polarized beam. Distributions of surface current and the corresponding chiral response of Weyl metamaterial under RCP and LCP incidence at Weyl frequency are illustrated in Figs. 4(c) and 4(d) in the same scale, respectively. The difference in the surface current oscillations on the Weyl unit-cell structure indicates its intrinsic chiral-optical behavior due to different multipole excitations when illuminated with different spin states. First in Fig. 4(c), a double circular surface current loop oscillation with C_2 rotation symmetry is induced on the unit cell excited by RCP, which corresponds to a magnetic dipole moment along the $(-\mathbf{u}-\mathbf{v})$ direction. The two locations where the electrical current switches directions indicate strong charge accumulation, which corresponds to the presence of an electrical dipole moment along the same direction. Consequently, the aligned electric and magnetic dipole along the same direction causes a chiral response. The strong resonant condition for RCP excitation arises from constructive interference between the excited magnetic dipole and the electric dipole moments, which leads to a strong scattering (reflection) and weak transmittance around the Weyl frequency.

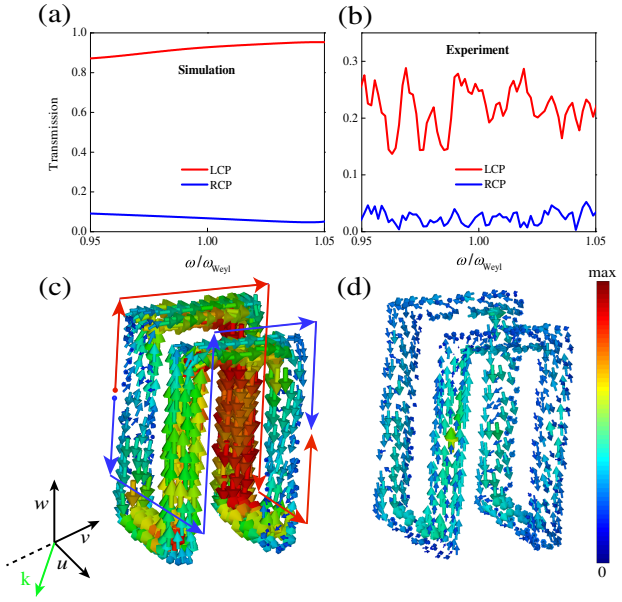

Fig. 4. Selective transmissions of circular polarized waves through the photonic Weyl metacrystal around the Weyl frequency. (a) Simulation results; (b) experimental measurement; surface current distributions and corresponding chiral response of Weyl metamaterial under RCP and LCP irradiance at Weyl frequency are, respectively, shown in (c) and (d). The unit wave vector of the incident beam is $1/\sqrt{2}(\vec{u}-\vec{v})$, which is denoted by the green vector. The double circular surface current loop oscillations denoted by red and blue arrows on the Weyl structure in (c) indicate its intrinsic chiral-optical response when illuminated by the circular polarized wave with the same chiral spin states.

On the other hand, for LCP excitation, as shown in Fig. 4(d), there is a much weaker interaction between the unit cell and the incident wave, which is due to a destructive interference between the induced magnetic dipole and the electric dipole moments. Consequently, the LCP light could transmit through the Weyl metamaterial with very high transmission [55]. Thus, the Weyl metamaterial provides a straightforward strategy for achieving 3D chirality and potential applications in spin optical manipulations and photon-spin selective devices.

4. CONCLUSIONS

In summary, we have experimentally realized the 3D Veselago lens based on an ideal photonic Weyl metamaterial, and the experimental observations are in good agreement with the simulation results. In comparison to a negative refractive index medium that operates close to the resonance frequencies, the Weyl medium operates far from the resonance, as indicated by the linear dispersion of the Weyl cone. Therefore, the Weyl metamaterial is more robust to disorders and intrinsic losses. Furthermore, the Weyl approach towards negative refraction provides major advantages over traditional negative-index metamaterial due to the simplicity of the structural design. Our research findings may provide a route for various imaging applications and spin optical signal processing.

APPENDIX A

Sample configuration of Weyl metacrystal is shown in Fig. 5(a). The saddle-shaped metallic structures with D_{2d} point group symmetry are etched in the 3-mm-thick hosting material with a dielectric constant of 2.2. The detailed feature is shown in the inset. The experimental setup for the detection of negative refraction is shown in Fig. 5(b). The sample is stacked layer by layer to form a 3D Weyl metacrystal, where between two structured layers there is a 1.5-mm-thick spacer with the same dielectric constant. One antenna is working as the source dipole and another antenna is used

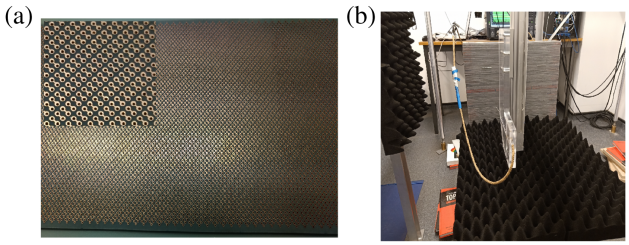

Fig. 5. (a) Top view of the Weyl metamaterial that is fabricated by a printed circuit board. The inset on the upper-left corner shows the detailed feature; (b) experimental setup for the measurement of negative refraction.

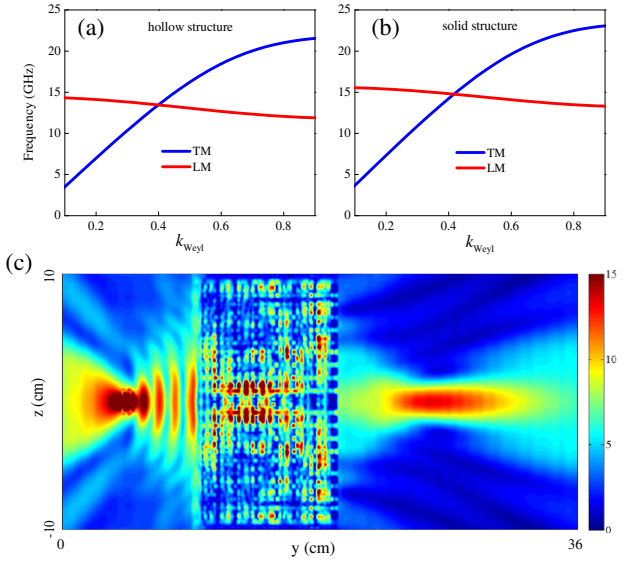

Fig. 6. (a), (b) Band structures of Weyl metamaterial that are composed of solid and hollow cylinders, respectively; (c) simulated all-angle negative refraction in the yz plane of the ideal Weyl metacrystal.

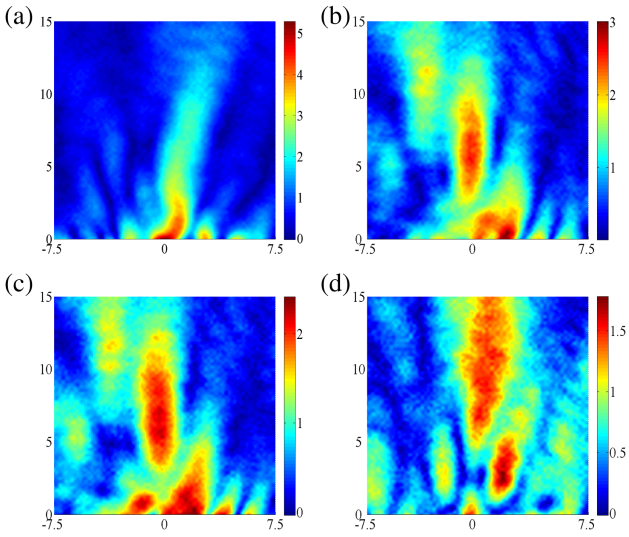

Fig. 7. Evolution of the focusing profile of the transmitted wave across the Weyl metacrystal with the incident dipole polarized along the x direction when the frequency approaches the Weyl frequency.

as a probe. A black foam is placed underneath the sample to serve as an absorber to reduce the scattering of waves.

The band structures of the ideal Weyl metacrystals that are composed of solid and hollow cylinders are shown in Figs. 6(a) and 6(b), respectively. The comparison between them shows they have very similar Weyl degeneracy, but with a slight frequency shift of about 1.2 GHz. The simulated beam focusing in the yz plane is illustrated in Fig. 6(c). It clearly shows that the incident beam is focused on the other side of the metacrystal, which is the same as that in the xy plane. It further confirms that our ideal Weyl metacrystal is capable of all-angle negative refraction in 3D.

In the full wave simulations of imaging by CST, the Weyl metamaterial consists of 35, 23, and 35 unit cells along the x, y, and z directions, respectively, where the number of unit cells along the y direction is the same as that in the experiment. In the simulation, the mesh size is carefully chosen such that the simulation result is converged with further refinement of the mesh size. Field monitors are used to record the electromagnetic field distributions.

The experimental measurements of the evolution of the transmitted wave through the Weyl metacrystal when the incident dipole is polarized along the x direction is shown in Fig. 7. It shows when the frequency increases to the Weyl frequency, the focusing spot moves gradually away from the interface and becomes elongated in the propagating direction (y direction). And when approaching the Weyl frequency, the focal spot spreads out, and the focal length increases towards infinity. The evolution of the beam focusing profile is similar to the other dipole polarization (Fig. 2) and is in good agreement with the full wave simulation results. It further demonstrates the great advantage of achieving Veselago lensing based on our ideal Weyl metamaterial, which is 3D, all-angle, broadband, and polarization-independent.

Funding. Fundamental Research Funds for the Central Universities; National Key Research and Development Program of China (2016YFA0301300); H2020 European Research Council (TOPOLOGICAL); National Natural Science Foundation of China (11874269, 61875133, 61875051); Natural Science Foundation of Zhejiang Province (LR21F010002).

Acknowledgment. S. Z. and Y. X. conceived the idea and supervised the project. Y. Y. and L. P. conducted the calculations and simulations. Y. Y. and Y. B. performed the experimental measurements. B. Y., S. M., H. C., and Y. X. shared valuable comments and suggestions. Y. Y., Y. X., and S. Z. prepared the report. All the authors discussed the results and commented on the article.

Disclosures. The authors declare no conflicts of interest.

†These authors contributed equally to the work.

REFERENCES

1. V. G. Veselago, "Electrodynamics of substances with simultaneously negative values of ε and μ," Usp. Fiz. Nauk **92**, 517–526 (1967).
2. J. B. Pendry, "Negative refraction makes a perfect lens," Phys. Rev. Lett.**85**, 3966–3969 (2000).
3. R. A. Shelby, D. R. Smith, and S. Schultz, "Experimental verification of a negative index of refraction," Science **292**, 77–79 (2001).
4. D. R. Smith, J. B. Pendry, and M. C. Wiltshire, "Metamaterials and negative refractive index," Science**305**, 788–792 (2004).
5. S. Zhang, W. Fan, N. Panoiu, K. Malloy, R. Osgood, and S. Brueck, "Experimental demonstration of near-infrared negative-index metamaterials," Phys. Rev. Lett. **95**, 137404 (2005).
6. V. M. Shalaev, W. Cai, U. K. Chettiar, H.-K. Yuan, A. K. Sarychev, V. P. Drachev, and A. V. Kildishev, "Negative index of refraction in optical metamaterials," Opt. Lett.**30**, 3356–3358 (2005).
7. J. Valentine, S. Zhang, T. Zentgraf, E. Ulin-Avila, D. A. Genov, G. Bartal, and X. Zhang, "Three-dimensional optical metamaterial with a negative refractive index," Nature **455**, 376–379 (2008).
8. C. M. Soukoulis and M. Wegener, "Past achievements and future challenges in the development of three-dimensional photonic metamaterials," Nat. Photonics**5**, 523–530 (2011).
9. S. Zhang, Y.-S. Park, J. Li, X. Lu, W. Zhang, and X. Zhang, "Negative refractive index in chiral metamaterials," Phys. Rev. Lett. **102**, 023901 (2009).
10. T. Xu, A. Agrawal, M. Abashin, K. J. Chau, and H. J. Lezec, "All-angle negative refraction and active flat lensing of ultraviolet light," Nature **497**, 470–474 (2013).
11. E. Cubukcu, K. Aydin, E. Ozbay, S. Foteinopoulou, and C. M. Soukoulis, "Negative refraction by photonic crystals," Nature**423**, 604–605 (2003).
12. C. Luo, S. G. Johnson, J. Joannopoulos, and J. Pendry, "Negative refraction without negative index in metallic photonic crystals," Opt. Express **11**, 746–754 (2003).
13. H. Shin and S. Fan, "All-angle negative refraction for surface plasmon waves using a metal-dielectric-metal structure," Phys. Rev. Lett.**96**, 073907 (2006).

14. H. J. Lezec, J. A. Dionne, and H. A. Atwater, "Negative refraction at visible frequencies," Science**316**, 430–432 (2007).
15. X. Lin, Y. Yang, N. Rivera, J. J. López, Y. Shen, I. Kaminer, H. Chen, B. Zhang, J. D. Joannopoulos, and M. Soljačić, "All-angle negative refraction of highly squeezed plasmon and phonon polaritons in graphene–boron nitride heterostructures," Proc. Natl. Acad. Sci. USA **114**, 6717–6721 (2017).
16. A. J. Hoffman, L. Alekseyev, S. S. Howard, K. J. Franz, D. Wasserman, V. A. Podolskiy, E. E. Narimanov, D. L. Sivco, and C. Gmachl, "Negative refraction in semiconductor metamaterials," Nat. Mater. **6**, 946–950 (2007).
17. J. Yao, Z. Liu, Y. Liu, Y. Wang, C. Sun, G. Bartal, A. M. Stacy, and X. Zhang, "Optical negative refraction in bulk metamaterials of nanowires," Science **321**, 930 (2008).
18. Y. Liu, G. Bartal, and X. Zhang, "All-angle negative refraction and imaging in a bulk medium made of metallic nanowires in the visible region," Opt. Express**16**, 15439–15448 (2008).
19. C. L. Kane and E. J. Mele, "Quantum spin Hall effect in graphene," Phys. Rev. Lett.**95**, 226801 (2005).
20. B. A. Bernevig, T. L. Hughes, and S.-C. Zhang, "Quantum spin Hall effect and topological phase transition in HgTe quantum wells," Science **314**, 1757–1761 (2006).
21. X. Wan, A. M. Turner, A. Vishwanath, and S. Y. Savrasov, "Topological semimetal and Fermi-arc surface states in the electronic structure of pyrochlore iridates," Phys. Rev. B**83**, 205101 (2011).
22. F. Haldane and S. Raghu, "Possible realization of directional optical waveguides in photonic crystals with broken time-reversal symmetry," Phys. Rev. Lett. **100**, 013904 (2008).
23. Z. Wang, Y. Chong, J. D. Joannopoulos, and M. Soljačić, "Observation of unidirectional backscattering-immune topological electromagnetic states," Nature **461**, 772–775 (2009).
24. A. B. Khanikaev, S. H. Mousavi, W.-K. Tse, M. Kargarian, A. H. MacDonald, and G. Shvets, "Photonic topological insulators," Nat. Mater.**12**, 233–239 (2013).
25. M. C. Rechtsman, J. M. Zeuner, Y. Plotnik, Y. Lumer, D. Podolsky, F. Dreisow, S. Nolte, M. Segev, and A. Szameit, "Photonic Floquet topological insulators," Nature**496**, 196–200 (2013).
26. Y. Yang, Z. Gao, H. Xue, L. Zhang, M. He, Z. Yang, R. Singh, Y. Chong, B. Zhang, and H. Chen, "Realization of a three-dimensional photonic topological insulator," Nature **565**, 622–626 (2019).
27. C. He, H.-S. Lai, B. He, S.-Y. Yu, X. Xu, M.-H. Lu, and Y.-F. Chen, "Acoustic analogues of three-dimensional topological insulators," Nat. Commun. **11**, 2318 (2020).
28. L. Lu, L. Fu, J. D. Joannopoulos, and M. Soljačić, "Weyl points and line nodes in gyroid photonic crystals," Nat. Photonics **7**, 294–299 (2013).
29. L. Lu, Z. Wang, D. Ye, L. Ran, L. Fu, J. D. Joannopoulos, and M. Soljačić, "Experimental observation of Weyl points," Science**349**, 622–624 (2015).
30. W. Gao, M. Lawrence, B. Yang, F. Liu, F. Fang, B. Béri, J. Li, and S. Zhang, "Topological photonic phase in chiral hyperbolic metamaterials," Phys. Rev. Lett. **114**, 037402 (2015).
31. B. Yang, Q. Guo, B. Tremain, R. Liu, L. E. Barr, Q. Yan, W. Gao, H. Liu, Y. Xiang, and J. Chen, "Ideal Weyl points and helicoid surface states in artificial photonic crystal structures," Science**359**, 1013–1016 (2018).
32. Q. Guo, B. Yang, L. Xia, W. Gao, H. Liu, J. Chen, Y. Xiang, and S. Zhang, "Three dimensional photonic Dirac points in metamaterials," Phys. Rev. Lett. **119**, 213901 (2017).
33. H. He, C. Qiu, L. Ye, X. Cai, X. Fan, M. Ke, F. Zhang, and Z. Liu, "Topological negative refraction of surface acoustic waves in a Weyl phononic crystal," Nature**560**, 61–64 (2018).
34. X. Huang, Y. Lai, Z. H. Hang, H. Zheng, and C. Chan, "Dirac cones induced by accidental degeneracy in photonic crystals and zero-refractive-index materials," Nat. Mater.**10**, 582–586 (2011).
35. G.-G. Liu, P. Zhou, Y. Yang, H. Xue, X. Ren, X. Lin, H.-X. Sun, L. Bi, Y. Chong, and B. Zhang, "Observation of an unpaired photonic Dirac point," Nat. Commun.**11**, 1873 (2020).
36. M. Xiao, W.-J. Chen, W.-Y. He, and C. T. Chan, "Synthetic gauge flux and Weyl points in acoustic systems," Nat. Phys. **11**, 920–924 (2015).
37. M. Xiao, Q. Lin, and S. Fan, "Hyperbolic Weyl point in reciprocal chiral metamaterials," Phys. Rev. Lett. **117**, 057401 (2016).
38. B. Yang, Q. Guo, B. Tremain, L. E. Barr, W. Gao, H. Liu, B. Béri, Y. Xiang, D. Fan, A. P. Hibbins, and S. Zhang, "Direct observation of topological surface-state arcs in photonic metamaterials article," Nat. Commun.**8**, 97 (2017).
39. Y. Yang, J.-P. Xia, H.-X. Sun, Y. Ge, D. Jia, S.-Q. Yuan, S. A. Yang, Y. Chong, and B. Zhang, "Direct observation of topological surface-state arcs in photonic metamaterials," Nat. Commun.**10**, 97 (2019).
40. Q. Wang, M. Xiao, H. Liu, S. Zhu, and C. T. Chan, "Optical interface states protected by synthetic Weyl points," Phys. Rev. X **7**, 031032 (2017).
41. K. Halterman, M. Alidoust, and A. Zyuzin, "Epsilon-near-zero response and tunable perfect absorption in Weyl semimetals," Phys. Rev. B **98**, 085109 (2018).
42. R. D. Hills, A. Kusmartseva, and F. Kusmartsev, "Current-voltage characteristics of Weyl semimetal semiconducting devices, Veselago lenses, and hyperbolic Dirac phase," Phys. Rev. B **95**, 214103 (2017).
43. M. Yang, Q.-T. Hou, and R.-Q. Wang, "Electronic non-coplanar refraction and deflected diffraction of Weyl-node-mismatch junctions," New J. Phys.**21**, 113057 (2019).
44. M. Yang, Q.-T. Hou, and R.-Q. Wang, "Vortex of beam shift induced by mono-chiral interface states," New J. Phys. **22**, 033015 (2020).
45. M. Lu and X.-X. Zhang, "Electronic scattering, focusing, and resonance by a spherical barrier in Weyl semimetals," J. Phys. Condens. Matter**30**, 215303 (2018).
46. H. Cheng, W. Gao, Y. Bi, W. Liu, Z. Li, Q. Guo, Y. Yang, O. You, J. Feng, H. Sun, J. Tian, S. Chen, and S. Zhang, "Vortical reflection and spiraling Fermi arcs with Weyl metamaterials," Phys. Rev. Lett. **125**, 093904 (2020).
47. Y. Yang, W. Gao, L. Xia, H. Cheng, H. Jia, Y. Xiang, and S. Zhang, "Spontaneous emission and resonant scattering in transition from type I to type II photonic Weyl systems," Phys. Rev. Lett.**123**, 033901 (2019).
48. M. Zhou, L. Ying, L. Lu, L. Shi, J. Zi, and Z. Yu, "Electromagnetic scattering laws in Weyl systems," Nat. Commun.**8**, 1388 (2017).
49. Q.-D. Jiang, H. Jiang, H. Liu, Q.-F. Sun, and X. Xie, "Topological Imbert-Fedorov shift in Weyl semimetals," Phys. Rev. Lett. **115**, 156602 (2015).
50. U. Chattopadhyay, L.-K. Shi, B. Zhang, J. C. Song, and Y. D. Chong, "Fermi-arc-induced vortex structure in Weyl beam shifts," Phys. Rev. Lett. **122**, 066602 (2019).
51. H. Jia, R. Zhang, W. Gao, Q. Guo, B. Yang, J. Hu, Y. Bi, Y. Xiang, C. Liu, and S. Zhang, "Observation of chiral zero mode in inhomogeneous three-dimensional Weyl metamaterials," Science**363**, 148–151 (2019).
52. V. Peri, M. Serra-Garcia, R. Ilan, and S. D. Huber, "Axial-field-induced chiral channels in an acoustic Weyl system," Nat. Phys. **15**, 357–361 (2019).
53. A. A. Soluyanov, D. Gresch, Z. Wang, Q. Wu, M. Troyer, X. Dai, and B. A. Bernevig, "Type-II Weyl semimetals," Nature**527**, 495–498 (2015).
54. Q. Guo, W. Gao, J. Chen, Y. Liu, and S. Zhang, "Line degeneracy and strong spin-orbit coupling of light with bulk bianisotropic metamaterials," Phys. Rev. Lett.**115**, 067402 (2015).
55. S. Yang, Z. Liu, S. Hu, A.-Z. Jin, H. Yang, S. Zhang, J. Li, and C. Gu, "Spin-selective transmission in chiral folded metasurfaces," Nano Lett. **19**, 3432–3433 (2019).